Published in final edited form as:
Soft Matter. 2012 July 7; 8(25): 6713–6722. doi:10.1039/C2SM25373A.

X-ray diffraction study of nanocrystalline and amorphous structure within major and minor ampullate dragline spider silks

Sujatha Sampath[a], **Thomas Isdebski**[a], **Janelle E. Jenkins**[†,a], **Joel V. Ayon**[a], **Robert W. Henning**[b], **Joseph P. R. O. Orgel**[c], **Olga Antipoa**[c], and **Jeffery L. Yarger**[a]

Sujatha Sampath: sujatha.sampath@asu.edu; Jeffery L. Yarger: jyarger@gmail.com

[a]Department of Chemistry and Biochemistry, Magnetic Resonance Research Center, Arizona State University, Tempe, AZ, 85287-1604, USA

[b]Center for Advanced Radiation Sources, The University of Chicago, Chicago, IL 60637, USA

[c]Department of Biological and Chemical Sciences, Pritzker Institute of Biomedical Science and Engineering, Illinois Institute of Technology, Chicago, IL 60616, USA

Abstract

Synchrotron X-ray micro-diffraction experiments were carried out on *Nephila clavipes* (NC) and *Argiope aurantia* (AA) major (MA) and minor ampullate (MiA) fibers that make up dragline spider silk. The diffraction patterns show a semi-crystalline structure with β-poly(L-alanine) nanocrystallites embedded in a partially oriented amorphous matrix. A superlattice reflection 'S' diffraction ring is observed, which corresponds to a crystalline component larger in size and is poorly oriented, when compared to the β-poly(L-alanine) nanocrystallites that are commonly observed in dragline spider silks. Crystallite size, crystallinity and orientation about the fiber axis have been determined from the wide-angle X-ray diffraction (WAXD) patterns. In both NC and AA, the MiA silks are found to be more highly crystalline, when compared with the corresponding MA silks. Detailed analysis on the amorphous matrix shows considerable differences in the degree of order of the oriented amorphous component between the different silks studied and may play a crucial role in determining the mechanical properties of the silks.

1. Introduction

Spider silk is a remarkable biopolymer, a lightweight protein fiber that spiders produce for diverse purposes including web structure, prey immobilization, making egg cases and which is a key to their survival.[1,2] With a unique combination of high elasticity, mechanical strength and toughness, its superior material properties surpass those of any currently known man-made fiber.[1-4] In addition, these fibers are biocompatible and biodegradable.[5,6] It is one of the best examples of block copolymers in Nature in which repeating structural motifs are linked together covalently resulting in polymers that organize themselves into a variety of nano-structures with exceptional material properties.[7-10]

The extraordinary mechanical properties have been attributed to the hierarchical structuring at the nanometre length scales, and are designed to perform different functions at each level, effectively linking nano-scale constituents to properties at the macro level, a strategy often used in Nature (silk, bone, wood).[2-4,11] These features coupled with potential diverse applications render spider silk as an ideal model for biomimetic research. Over the last few

Correspondence to: Sujatha Sampath, sujatha.sampath@asu.edu; Jeffery L. Yarger, jyarger@gmail.com.
[†]Present address: Department of Nanostructured and Electronic Materials, Sandia National Laboratories, Albuquerque, NM 87185, USA

years there has been a great deal of interest in understanding how this nano-structuring works, both from a theoretical and experimental perspective, made feasible with the advent of more advanced experimental and computational facilities.[12-15] Recent advances in bioengineering have made considerable progress in the production of synthetic silks, however, to date synthetic fibers do not exhibit the same physical or mechanical properties of natural spider silk.[16-18] The viable production and use of these proteins as synthetic materials requires greater knowledge of the secondary, tertiary, and quaternary structure of the proteins that comprise spider silk.

About 125 million years ago, the *Araenoidea* superfamily of spiders diverged into the *Araneidae* (includes orb weavers *Araneus gemmoides, Argiope argentata*, and *Argiope aurantia*) and the "*derived araneoids*" (orb weaver *Nephila clavipes* and cobweb weavers *Latrodectus hesperus*).[19] All five species listed above have evolved to make six different types of silk fibers and an aqueous glue[19,20] with each silk having a specific function.[21,22]

Although the silks of various species serve the same general purposes, the mechanical properties differ slightly for each silk of a given species, allowing them to adapt to their unique ecosystems. Of all the different silk fibers, dragline silk (major ampullate silk) has shown the greatest mechanical variation between individual species.[23,24] The mechanical property variation in dragline silks can be partially attributed to the nanostructure composite nature of major ampullate spidroin 1 (MaSp1) and major ampullate spidroin 2 (MaSp2) proteins that make up dragline fibers.[25,26] Both MaSp1 and MaSp2 have evolutionarily conserved highly repetitive motif structures found in a large class of web building spiders.[27]

In order to understand what makes spider silks mechanically superior, it is imperative to understand the structural organization of the silk fibers. X-ray fiber diffraction has been a very useful technique to study the fiber structure at the molecular and atomic length scales.[13,28]

Previous X-ray studies[29-32] have shown the molecular organization of spider silks to consist of a semi-crystalline structure in which nano-crystallites made up of β-pleated sheets embedded in an amorphous matrix. The major focus of these studies has centered on the crystalline fraction of the spider silk. Most of these studies have been done on the silks spun primarily from a few species in the *Nephila* genera.

The dragline silk produced by the major ampullate (MA) glands which has been studied the most, is used for building the frame and radii of the orb-web as well as dragging an ever-present safety line, which is important, for example, when escaping predators.[11,22] While there is more understanding on the β-sheet nano-crystallites as regards its size, orientation about the fiber axis[29] and its role in acting as a crosslink between the network of protein chains in the amorphous matrix,[11,14] much less is known about the amorphous matrix itself and its role in the observed mechanical properties. With the amorphous matrix making up about 50–70% of the spider silk composition, it is very crucial to understand the structural aspects of this component and its correlation to the mechanical properties so as to be able to get a full understanding of the silk structure.

Motivation for the work in this paper is twofold: to compare the structural differences of silks spun by the major and minor ampullate (MiA) glands, both of which are used in web formation. The second focus of this study has been to understand the effect of the ratio of the two proteins MaSp1/MaSp2 in determining the silk properties. Towards this goal we have studied MA and MiA silks from two species, *Nephila clavipes* from the *derived Araneoidea* family and the other, *Argiope aurantia*, from the *Araneoidea* family, which is also a species with a different MaSp1/MaSp2 ratio and a higher content of one important amino acid, proline.[33]

2. Experimental

Spider specimen and forced silking techniques

Spiders of two different species – *Argiope aurantia* (AA) and *Nephila clavipes* (NC), were forcibly silked at a rate of 2 cm s^{-1} to collect silks from both the major (MA) and minor (MiA) ampullate glands.[34] Silking was performed under a dissection microscope to ensure that the MA and MiA silks were separated during the entire process. Spiders were silked every other day on average and were fed a cricket during silking. It is to be noted that spiders produce MiA silks in much lesser quantity than the MA silks.[34]

Gland material—*Nephila clavipes* MA glands were dissected from recently dead (within 30 minutes) adult female spiders. The dissections were performed under an optical microscope. The MA gland was easily identified by its location in the abdomen, as well as by the size and shape of the gland. DI water was utilized to irrigate the abdomen during dissection to prevent dehydration of the abdomen. The MA glands were carefully removed to prevent any puncturing and placed onto a glass slide for drying. The glass slides were then put into a covered beaker to prevent dust and other contaminates from sticking to the gland. The glands were then dried at ambient temperature and pressure. Once dried, the glands were carefully removed from the glass slide with a razor blade to ensure that the gland remained in a single piece. The glands were then mounted on metal washers. To mount the gland, the main section of the gland was centered over the hole in the washer and small amounts of superglue were utilized to tack the gland ends onto the washer. Care was taken to prevent any glue from contaminating the detection area of the gland.

Scanning electron microscopy (SEM)

The silk samples were prepared by mounting the fibers onto a sample stub with the use of double sided carbon tape. To prevent charging, the samples were placed into a gold coater (Denton Vacuum Sputter Coater Desk II) for 180 seconds to give an estimated 15 nm gold layer on the samples. The samples were then placed into the SEM specimen chamber (XL30 ESEM-FEG, FEI). The images were taken in Hi-Vac mode with a vacuum of 9×10^{-5} mbar. The electron beam (20 kV) had a beam diameter of 1.3 nm and a beam current of 148 pA. All images were recorded with a line time of 66.4 ms, with 484 lines per frame.

Wide angle X-ray diffraction (WAXD)

X-ray fiber diffraction was performed on the BioCARS 14BM-C beamline at the Advanced Photon Source at Argonne National Laboratory, Argonne, IL, USA. The wavelength of the X-ray beam was 0.9 Å with a flux of 6×10^{11} photons per second and the beam size on the sample was 150 × 200 μm. Data were recorded using an ADSC Quantum-315 detector. A bundle of 20–40 individual fibers of the MA silks and 10–20 individual fibers of the MiA silks were held taut (but unstretched) in a metal frame, with the fiber axis normal to the X-ray beam. The sample to detector distance was 200 mm. Since the scattered intensity from MA silks was in general higher than that obtained from MiA silks, data collection times varied accordingly, 30 s for one image for the MA silk and 60 s for the MiA silk. Background measurement was performed with the sample displaced from the beam and the image was recorded under the same conditions as used with the sample in the beam. Multiple images were taken to get better statistics and improve on the signal/background ratio. CeO_2 powder was used for instrument calibration. The 2D WAXD patterns were analysed using the software package FIT2D.[35] Radial and azimuthal 1D profiles were obtained from the deconvolution of 2D WAXD images using FIT2D. Radial profiles are intensity as a function of radius integrated azimuthally over a sector typically 20–30 degrees wide, while azimuthal profiles are integrated intensity as a function of all azimuthal angles over a very thin annular ring centered at the peak maximum of the desired reflection.[29,30]

Microcal Origin was used for the deconvolution of the 1D X-ray data and peak fitting. The peaks were fitted with Gaussian functions using nonlinear least squares fitting. Like previous X-ray diffraction analyses on spider silks, sequential analysis instead of whole pattern fitting has been applied.[29]

3. Results and discussion

Nephila clavipes: major and minor ampullate silks

In Fig. 1 the SEM images of MA and MiA fibers of *Nephila clavipes* (A and B respectively) are shown. Uniformity of the cylindrical fibers along the length of the fibers is observed for both the MA and MiA fibers. Differences between major and minor strands of both species are observed through varied diameters, with major fibers ranging between 3 and 3.5 μm and minor fibers ranging between 1.3 and 1.6 μm.

The WAXD pattern of NC MA silk is shown in Fig. 2a. The diffraction pattern resembles those from previous reports[29-32] and depicts a semi-crystalline structure characterized by crystalline-Bragg reflections and an amorphous fraction. The predominant structural model for spider silk fiber is that it contains a crystalline component, an oriented and an isotropic amorphous component.[29-32] The crystalline reflections are broad due to the small size of the crystallites.[29] Intense reflections are observed along the equator (perpendicular to the fiber axis). Also observed are higher order layer-line reflections, parallel to the equator. Along the meridian (parallel to the fiber axis) the main (002) reflection is strong, while subsequent higher order reflections are weaker. The reflections comprising the crystalline fraction correspond to the pattern of β-poly(L-alanine) structure.[29-32] The reflections were indexed based on an orthogonal unit cell with the *c*-axis as the fiber axis.[36] Also observed is a strong powder-like diffraction ring at ~4.2 Å with a stronger intensity along the meridian, marked as the 'S' or the superlattice reflection.[32,37] This feature is from a crystalline component different from the β-sheet nano-crystallites, as is described in later sections.[32,37]

Fig. 2b shows the WAXD pattern of NC MiA silk from the same spider from which the MA silk was silked. To the best of the authors' knowledge, this is the first high resolution X-ray diffraction pattern of the MiA silk reported so far. Qualitatively the pattern is similar to that of NC MA silk, in that it has semi-crystalline structure with crystalline reflections embedded in an amorphous matrix. The crystalline fraction of the MiA silk also corresponds to β-poly(L-alanine) structure as in MA silk. The *d*-spacings of the MiA silk crystalline reflections are close to that of the MA silk as shown in Table 1. Scaled relative intensities obtained from the total integrated intensity of the whole 2D pattern are also shown in Table 1. Though MA silks from NC and other species have been the subject of both structural and mechanical properties studies previously, MiA silks have not been studied much. The primary reason is that MiA silk collection is more difficult because of the smaller size of the MiA gland and second, that MiA silk is thinner than a MA silk fiber resulting in a weaker scattered intensity in an WAXD experiment and hence requiring more silk for better signal/noise ratio.

According to the prevalent structural model for spider silk, it has a hierarchical structure with each silk fiber being composed of many fibrils and each fibril in turn being composed of anisotropic nano-crystalline domains connected by an amorphous matrix, which has both an oriented and an isotropic component.[12,29,32] Crystallite size, orientation distribution of the crystallites about the fiber axis, and the percentage crystallinity in the silk fiber can be determined from WAXD. Analysis of the main equatorial reflections (200), (120) and the main meridian reflection (002) gives the crystallite size in the *a, b*, and *c* directions respectively.[29,32,38]

Crystallite size and crystallinity

Radial integration along the equator and meridian gives the radial peak width of the equatorial (200), (120) and meridional (002) reflections.[39,40,45] Fig. 3a shows the 1D radial intensity profile along the equator which has been integrated azimuthally over a sector to include the two main equatorial Bragg reflections (200)/(120) (as shown in the inset) for the NC MA silk. The inner weaker (200) peak on the equator corresponds to the distance between β-sheets and is denoted as the *a*-axis of the crystallite while the outer stronger (120) peak corresponds to the interchain distance and is denoted here as the *b*-axis of the crystallite.[29,38] The (002) peak on the meridian corresponds to the size of the crystallite in the *c* direction, along the fiber axis. The 1D equatorial radial-profile has been deconvoluted into two crystalline peaks and an amorphous peak, by fitting with Gaussian peaks for the Bragg reflections, a broader Gaussian peak for the amorphous component (includes both oriented and unoriented). The intensity at 20° from the equator is almost entirely from the amorphous halo which has been used as a constraint for the amorphous peak in the fitting process. The radial width of the inner (200) peak is wider than that of the outer (120) peak, implying that the crystallites are thinner perpendicular to the hydrogen-bonded planes (200), as has been seen with other silks.[29,39,40] Fig. 3b shows the 1D radial intensity profile of the (002) meridional peak for MA silk. The signal intensity of this peak was weak as compared to the equatorial peak intensities. The shape of the (002) peak as a function of diffraction angle is asymmetric at higher angles, due to overlap with other layer-line reflections.[29] This peak has been fitted using two Gaussians: one for the crystalline component and a broader Gaussian for the amorphous halo. Average sizes of the crystallites along the *a, b* and *c* axes have been determined by using Scherrer's formula.[41] The average crystallite size was found to be 2.65, 3.97, and 7.05 nm along the *a, b* and *c* directions.

The degree of crystallinity x_c was estimated from the radial intensity profile of the strongest equatorial reflections (200)/(120) (Fig. 3a) using the relation $x_c = (I_c/I_c + I_a)$, I_c is the sum of the integrated intensities of the (200) and (120) crystalline peaks and I_a is the integrated intensity of the amorphous halo.[42] This results in a value of 28% for the crystalline fraction in MA silk. It has been demonstrated by Grubb and Jelinski[29] that crystallinity calculated from the whole pattern and that from the sequential method[29-33,38] (considering only the main equatorial peaks (200)/(120)) are in good agreement.

Figs. 3c and 3d show the 1D radial profiles of the (200)/(120) and (002) peaks for the NC MiA silk. The peak at higher angles (Fig. 3c) is due to overlap of weaker peaks, not seen in MA silk. From Fig. 3c, it is seen that the (200) peak is sharper than it is in the MA silk. The analysis of the peaks and the calculation of the crystalline parameters have been done in a similar manner as described for the NC MA silk. The average crystallite size was found to be 2.62, 4.02, and 10.1 nm along the *a, b* and *c* directions. It is to be noted that the size of the MiA silk crystallites in the *c* direction (size along the fiber axis) is larger than in the MA silk, while their size in the *a* and *b* directions is comparable in both silks.

The degree of crystallinity x_c was estimated from the radial intensity profile of the strongest equatorial reflections (200)/(120) (Fig. 3c) using the method as was used for MA silk yields a value of 36% for the crystalline fraction in MiA silk. These results show that not only are the crystallites larger in the MiA silk, but its % crystallinity is significantly higher than MA silk as well.

Orientational order

The axial orientation distribution of the crystallites about the fiber axis was determined from azimuthal broadening (FWHM) of the (200)/(120) equatorial reflections. Orientational order can be expressed quantitatively in terms of Herman's orientation function $f_c = (3\langle \cos 2\varphi \rangle -$

1)/2, where φ is the angle between the c axis and the fiber axis.[43] The parameter f_c is 0 for no preferred orientation in fibers and 1 if all crystallites are perfectly aligned with respect to each other. $\langle\cos^2\varphi\rangle$ can be obtained from azimuthal width of the two strongest equatorial reflections (200)/(120) based on the equation[29,32,38] $\langle\cos^2\varphi\rangle = 1 - A\langle\cos^2\varphi_1\rangle - B\langle\cos^2\varphi_2\rangle$, where $A = 0.8$, $B = 1.2$.

Fig. 4a is a plot of the intensity as a function of angle measured from the equator at the radial position of the strong (120) peak, and Fig. 4b is the corresponding plot at the position of the (200) peak. (The annular region used for integration is shown in the insets.) Both (120) and (200) peaks have been fitted with two Gaussian functions, one wider than the other, according to the structural model used in previous studies on spider silks.[29,32] It has been shown by Grubb and Jelinski[29] that the narrower Gaussian dominates at the equator and corresponds to the crystalline material (I_{120} or I_{200}), and the broader Gaussian corresponds to the oriented amorphous material, which dominates about 20° off the equator. In the case of the (120) peak profile, small subsidiary peaks due to residual intensity from the (201) reflections were treated as individual Gaussian functions. The degree of orientation of both the crystalline and the oriented amorphous material has been determined from their FWHM as described above.[29,32] The calculated value of the orientation function for the crystalline material is $f_c \approx 0.985$ and ≈ 0.8 for the oriented amorphous material, for NC MA silk.

Figs. 4c and 4d show the azimuthal scans at the radial position of the (120) and (200) peaks respectively of the MiA silk. In general, the (200) is broader than the (120) for both the MA and the MiA silks. The peak fitting and the determination of orientation functions have been performed as described for the MA silk and the values are ~0.975 and 0.75 for the crystalline and the oriented amorphous material respectively. In the MA silk, both the crystallites and the oriented amorphous fraction are better oriented than in the MiA silk, while the MiA is more crystalline than the MA silk. The values for the MA silk are comparable to those obtained by previous studies on the NC MA silk,[29] to the best of the authors' knowledge there are no reports for these values for the MiA silk. The crystallinity parameters and the orientation function values for the crystalline and the amorphous material are listed in Table 2.

Superlattice reflection

In the 2D WAXD patterns (Figs. 2a and 2b) of both MA and MiA silks a diffuse ring with a strong meridional intensity at ~4.2 Å is seen, which does not belong to the β-poly(L-alanine) structure. This reflection has been called the superlattice reflection (S) in previous works.[32,37] It is to be noted that the term 'superlattice' however does not refer to a superstructure in the crystallographic perspective. Fig. 5a shows the azimuthal intensity profile centered at the radial position of the S reflection, for NC MA silk. The inset in Fig. 5a shows the radial intensity profile of the S reflection along with the (002) reflection. The S and the (002) peaks have been deconvoluted from the broad background using Gaussian fits. The radial width of the S reflection is smaller than that of (002) indicating that the crystalline component contributing to the S reflection is larger in size than the β-sheet nano-crystallites. The azimuthal width of the S reflection is broader than that of (002). This indicates that the axial orientational order of the crystalline component giving rise to the S reflection is lower than that of β-sheet crystallites. Fig. 5b shows the azimuthal intensity profile centered at the radial position of the S reflection and the inset shows the radial intensity profile of the S and the (002) reflection for NC MiA silk. Similar to MA silk, while the radial width of the S reflection is smaller, the azimuthal width is broader than the (002) reflection indicating a larger and less oriented crystalline component than the β-sheet crystallites. However comparing the S reflection between the MA and MiA silks, the ratio of the integrated intensities of the $I_{(002)}/I_{(S)}$ is smaller in MA than in MiA silk, suggesting that

the S crystalline component is larger in MA silk compared to MiA silk (Table 2). In addition the azimuthal peak width of the S reflection is slightly smaller in MiA silk compared to MA silk, implying that the S reflection has better axial ordering in MiA silk than in MA silk.

The presence of larger ordered regions in MA silk other than β-sheet crystallites has been observed by TEM by Thiel and coworkers[44-46] and explained as "*Non Periodic Lattice (NPL) crystals which form as a result of statistical matches between compatible sequences on adjacent molecular chains*". There have been few other reports from X-ray studies indicating the presence of a second crystalline component which is larger in size and less oriented about the fiber axis than the β-sheet crystallites.[32,37,47] From our data, the presence of a superlattice reflection in both MA and MiA silks from *Nephila clavipes* and in silks from another species, *Argiope aurantia* (discussed in later sections), clearly indicate the presence of another crystalline component besides the β-sheet nano-crystallites. However, determination of the size and shape of the S crystalline component is outside the range of length scales that can be determined from wide angle scattering measurements. Further work has to be done with techniques like small angle X-ray/neutron scattering, which can help determine the size and shape of larger crystallites.

Major ampullate dehydrated gland material

Figs. 5c and 5d show the WAXD pattern and the corresponding 1D integrated radial profile of the whole pattern of the dehydrated gland material from the *Nephila clavipes* MA gland. Concentric diffraction rings seen in the WAXD pattern and the integrated 1D profile has peaks that occur at the same *d*-spacing values as the main principal crystalline reflections (corresponding to β-sheet crystallites) in the fiber, which is a significant finding. The peaks in the dehydrated gland material correspond to the *d*-spacings of the equatorial and layer-line reflections, but not to the meridional reflections in the fiber, which we interpret as arising from a secondary structure which has a certain degree of order but no preferred orientation.

Argiope aurantia (AA): major and minor ampullate silks

In order to understand how the silk properties depend on the ratio of MaSp1/MaSp2 and MiSp1/MiSp2, we studied the MA and MiA silks of another species, *Argiope aurantia* (AA). The proline content of AA is known to be significantly higher than that found in *Nephila clavipes*.[33,34] Because proline is only found in the MaSp2 protein, it is deduced that a higher proline content corresponds to a larger fraction of MaSp2 in the AA MA silk fiber. The silks were obtained from AA spiders in a very similar manner to that described for NC. WAXD measurements and data analysis were carried out using the same procedure as discussed for NC silks.

Fig. 6 shows the SEM images of MA and MiA fibers of *Argiope aurantia* (A and B respectively). Uniformity of the cylindrical fibers along the length of the fibers is observed for both the MA and MiA fibers. Differences between major and minor strands are observed through varied diameters, with major fibers ranging between 3 and 3.5 μm and minor fibers ranging between 1.3 and 1.6 μm, similar to that found in NC MA and MiA silks.

Figs. 7a and 7b show the 2D WAXD patterns for the AA MA and MiA silks respectively. The diffraction patterns depict a semi-crystalline structure with crystalline Bragg reflections and an amorphous halo as in the case of the NC MA and MiA silks. The reflections comprising the crystalline fraction correspond to the pattern of β-poly(L-alanine) structure[29,32] and were indexed based on an orthogonal unit cell with the *c*-axis as the fiber axis.[36] The crystalline reflections in AA MA silk are sharper and better resolved spatially than in the AA MiA and NC MA silks. However, the (002) meridional reflection is stronger

in AA MiA than in the AA MA silk indicating the order along the meridian (fiber axis) is stronger, as seen in both AA and NC MiA silks, while the lateral order is better in the MA silks (both NC and AA). This could in part explain the higher ultimate strength of the MA silks (better structural ordering perpendicular to the fiber axis) and higher extensibility of MiA silks (better structural ordering parallel to the fiber axis) as observed in mechanical properties.[48] The superlattice reflection (S) is stronger in the AA MA silk compared to NC MA silk. The crystal size, crystallinity, orientation distribution of the crystallites and the oriented amorphous component have been calculated from analysis of the 1D radial profiles of the main equatorial peaks (200)/(120), the 1D azimuthal profiles at the peak position of the (120) and (200) peaks respectively, as performed for NC silks and their values listed in Table 2. Figs. 7c–j show the 1D radial and azimuthal profiles of the (200)/(120) and (002) peaks for the MA and MiA AA silks.

From Table 2 it is seen that AA MiA silk is more crystalline than the AA MA silk, the same trend observed between NC MA and MiA silks. This trend is in agreement with the quantitative correlation between the protein primary amino acid sequence and secondary structural motifs.[34] The linked poly-GA and poly-A regions of MiA silk are more abundant and have longer consecutive sequences than what is found in MA silk. The percentage of β-sheet determined from WAXD is still significantly lower than that determined by NMR. However, the trend toward minor ampullate silk being more crystalline is in good agreement with the NMR results.[34] While the degree of orientation of the crystallites is comparable in the AA MA and MiA silks, the oriented amorphous matrix is less oriented in the AA MA silk compared to the MiA silk, which is different from the trend observed in NC silks. Fig. 7k and l show the azimuthal intensity profile centered at the position of the S peak for MA and MiA silks respectively. The insets show the radial intensity profiles respectively. The S peak is the strongest in AA MA silk, among all the four silks studied here. In fact the S peak in AA MA is stronger than the (002) peak. In AA MiA silk, the S reflection is almost negligible which might be contributing to the better orientation of the oriented component of the amorphous matrix in AA MiA silk (Table 2).

Comparing MA silks between the two species, while AA MA silk is more crystalline than NC MA silk, the degree of orientation of its oriented amorphous component is much less when compared to NC MA silk. Studies comparing MA silks from different species have observed that while the mechanical properties are similar in the dry silk, considerable differences have been observed when the silk is wetted and the silk undergoes shrinking called ‘supercontraction’.[49-51] While most studies on spider silk have focused so far on the β-sheet crystallites, from this study the possible role of the amorphous matrix in determining its mechanical properties is becoming more evident. We conclude that the degree of orientation of the amorphous component is crucial in determining the mechanical properties of the silk, since this component could be regarded as the connecting interface between the β-sheet crystallites and the isotropic amorphous matrix.[11,37] The higher the degree of orientation of the oriented amorphous component, the better the mechanical properties of the silk seem to be. From the four different silks we have studied, there seems to be a correlation between the S crystalline component and the degree of orientation in the amorphous component. The stronger the S crystalline component, the poorer the orientation is in the oriented amorphous component. Further studies on silks from other spiders and other glands besides the MA and MiA glands are required to see if this is a general trend across all species.

4. Summary of results and conclusion

Spider silks from MA and MiA glands from two different species, *Nephila clavipes* and *Argiope aurantia*, have been studied using WAXD. The results obtained can be summarized as:

- **i.** The MiA silks from both species are more crystalline than their MA silks.
- **ii.** The β-sheet nanocrystallites are bigger in MiA silks than in MA silks (esp. in *c*-direction) in both species studied.
- **iii.** The β-sheet nanocrystallites are very well oriented about the fiber axis as seen from the calculated Herman's orientation function f_c having values ranging between 0.985 and 0.97 for the four silks (Table 2). While the orientation of the crystallites is comparable between MA and MiA silks in both species, the trend in $f_{\text{oriented-amorphous}}$ is not the same in MA and MiA silks of the two species (Table 2).
- **iv.** A crystalline phase different from the polyalanine β-sheet nanocrystallites has been observed in both MA and MiA silks called the superlattice component S. This component is bigger in size and poorly oriented about the fiber axis compared to the nanocrystallites.
- **v.** The S reflection is stronger in the MA silks in both NC and AA silks. While the NC MiA has a S reflection, this peak is almost negligible in the AA MiA. An interesting if not direct correlation is seen between the proline content and the S reflection, the strongest S peak occurs in the proline rich AA MA silk and the weaker S in the proline deficient NC MA and MiA silks and with AA MiA silk having no proline, the S peak is absent. Further studies on other species are needed to confirm if the trend seen here between proline content, S peak and the oriented amorphous matrix is a general trend.

Previous structural studies using X-ray/neutrons have been carried out on MA silks of the *Nephila* genera, their focus has mainly been the crystalline portion comprising the polyalanine β-sheet nanocrystallites. In this study, we have studied not only structural changes between silks from the MA and MiA glands of the same species (NC), but also from MA and MiA glands in a different species (AA) with a different MaSp1/MaSp2 ratio and a higher proline content. This has a twofold importance, the first is since spiders use silk from each of the six glands for a unique purpose, knowledge of the structure of each silk combined, with the knowledge of its chemical makeup, would help in designing synthetic polymers with different properties for different purposes. Second, studying silks from different species which have evolved at different times along the evolutionary chain where the spiders adapted to their ecological conditions to spin a fiber in relatively small time scales to suit their specific purpose, would give us a better idea of differences in the crystalline/amorphous ratio, the degree of orientation of both the crystalline and oriented amorphous components, and how they affected the resulting mechanical properties of silk. Detailed data analysis has elucidated that not only is the role of β-sheet nanocrystallites important in determining the superior properties of the spider silk, but rather, the degree of orientation of the oriented amorphous component, and the strength and nature of the superlattice crystalline component are crucial in determining the observed mechanical properties of the silk.

Acknowledgments

The Department of Defense Air Force Office of Scientific Research (AFOSR) under award no. FA9550-10-1-0275 and the National Science Foundation, Division of Materials Research under award no. DMR-0805197 supported this work. Use of the Advanced Photon Source was supported by the U.S. Department of Energy, Basic Energy Sciences, Office of Science, under contract no. DE-AC02-06CH11357 and DOE-EPSCoR under contract number

DE-SC0004791. Use of the BioCARS Sector 14 was supported by the National Institutes of Health, National Center for Research Resources, under grant number RR007707. Funding from National Science Foundation (grant #MCB-0644015 CAREER) and the National Institutes of Health (grant #RR-08630) is acknowledged. The authors would also like to thank Greg Holland, Florence Teulé and Randy Lewis for helpful discussions about spider silk materials.

References

1. Lewis RV. Chem Rev. 2006; 106:3762–3774. [PubMed: 16967919]
2. Vollrath F, Knight DP. Nature. 2001; 410:541–548. [PubMed: 11279484]
3. Heim M, Romer L, Scheibel T. Chem Soc Rev. 2010; 39:156–164. [PubMed: 20023846]
4. Eisoldt L, Smith A, Scheibel T. Mater Today. 2011; 14:80–86.
5. Gellynck K, et al. J Mater Sci: Mater Med. 2008; 19:2963–2970. [PubMed: 18360800]
6. Brown CP, Rosei F, Traversad E, Licocciaac S. Nanoscale. 2011; 3:870–876. [PubMed: 21212901]
7. Rabotyagova OS, Cebe P, Kaplan DL. Biomacromolecules. 2009; 10:229–236. [PubMed: 19128057]
8. van Beek JD, Hess S, Vollrath F, Meier BH. Proc Natl Acad Sci U S A. 2002; 99:10266–10271. [PubMed: 12149440]
9. Knight DP, Vollrath F. Philos Trans R Soc B. 2002; 357:155–163.
10. Qu Y, Payne SC, Apkarian RP, Conticello VP. J Am Chem Soc. 2000; 122:5014–5015.
11. Buehler MJ. Nano Today. 2010; 5:379–383.
12. Morris K, Serpell L. Chem Soc Rev. 2010; 39:3445–3453. [PubMed: 20668734]
13. Riekel C. Rep Prog Phys. 2000; 63:233–262.
14. Buehler MJ. Nat Nanotechnol. 2010; 5:172–174. [PubMed: 20190749]
15. Keten S, Buehler MJ. Appl Phys Lett. 2010; 96:153701–153703.
16. Lazaris A, Arcidiacono S, Huang Y, Zhou JF, Duguay F, Chretien N, Welsh EA, Soares JW, Karatzas CN. Science. 2002; 295:472–476. [PubMed: 11799236]
17. Brooks AE, Stricker SM, Joshi SB, Kamerzell TJ, Middaugh CR, Lewis RV. Biomacromolecules. 2008; 9:1506–1510. [PubMed: 18457450]
18. Seidel A, Liivak O, Jelinksi L. Macromolecules. 1998; 31:6733–6736.
19. Gatesy J, Hayashi C, Motriuk D, Woods J, Lewis RV. Science. 2001; 291(5513):2603–2605. [PubMed: 11283372]
20. Peters HM. Z Naturforsch A: Astrophys Phys Phys Chem. 1955; 10:395–405.
21. Vollrath F. Sci Am. 1992; 266:70–76.J Biotechnol. 2000; 74:67–83. [PubMed: 11763504]
22. Heim M, Keerl D, Scheibel T. Angew Chem Int Ed. 2009; 48:3584–3596.
23. Brooks AE, Steinkraus HB, Nelson SR, Lewis RV. Biomacromolecules. 2005; 6:3095–3099. [PubMed: 16283732]
24. Blackledge TA, Summers AP, Hayashi CY. Zoology (Jena). 2005; 108:41–46. [PubMed: 16351953]
25. Xu M, Lewis RV. Proc Natl Acad Sci U S A. 1990; 87:7120–7124. [PubMed: 2402494]
26. Hinman M, Lewis RV. J Biol Chem. 1992; 267:19320–19324. [PubMed: 1527052]
27. Hayashi CY, Shipley NH, Lewis RV. Int J Biol Macromol. 1999; 24:271–275. [PubMed: 10342774]
28. Stubbs G. Curr Opin Struct Biol. 1999; 9:615–619. [PubMed: 10508775]
29. Grubb DT, Jelinski LW. Macromolecules. 1997; 30:2860–2867.
30. Riekel C, Branden C, Craig C, Ferrero C, Heidelbach F, Muller M. Int J Biol Macromol. 1999; 24:179–186. [PubMed: 10342763]
31. Bram A, Branden CI, Craig C, Snigireva I, Riekel C. J Appl Crystallogr. 1997; 30:390–392.
32. Riekel C, Muller M. Macromolecules. 1999; 32:4464–4466.
33. Liu Y, Sponner A, Porter D, Vollrath F. Biomacromolecules. 2008; 9:116–121. [PubMed: 18052126]

34. Jenkins JE, Creager MS, Lewis RV, Holland GP, Yarger JL. Biomacromolecules. 2010; 11:192–200. [PubMed: 20000730]
35. Hammersley, A. FIT2D, http://www.esrf.fr/computing/expg
36. Warwicker JO. J Mol Biol. 1960; 2:350–362. [PubMed: 13783274]
37. Sheu H-S, Phyu KW, Jean Y-C, Chiang Y-P, Tso I-M, Wub H-C, Yang J-C, Ferng S-L. Int J Biol Macromol. 2004; 34:267–273.
38. Du N, Liu XY, Narayanan J, Li L, Lek M, Lim M, Li D. Biophys J. 2006; 91:4528–4535. [PubMed: 16950851]
39. Nadiger GS, Halliyal VG. Colourage. 1984; 31:23–32.
40. Kaplan, DL.; Lombardi, SJ.; Muller, WS.; Fossey, SA. Biomaterials: Novel Materials from Biological Sources. Byrom, D., editor. Stockton Press; New York: 1991. p. 2
41. Cullity, BD. Diffraction I: The Directions of Diffracted Beams. In: Cullity, BD., editor. Elements of X-Ray Diffraction. Vol. ch. 3. Addison-Wesley; Waltham, MA: 1959. p. 99
42. Alexander, LE. X-Ray Diffraction Methods in Polymer Science. Vol. ch. 3. Wiley-Interscience, John Wiley & Sons; 1969.
43. Stein, RS.; Wilkes, GL. Structure and Properties of Oriented Polymers. Ward, IM., editor. Applied Science Publishers Ltd; London: 1975. p. 70-84.
44. Thiel BL, Guess KB, Viney C. Biopolymers. 1997; 41:703–719. [PubMed: 9128438]
45. Thiel BL, Viney C. J Microsc. 1997; 185:179–187.
46. Barghout JYJ, Thiel BL, Viney C. Int J Biol Macromol. 1999; 24:211–217. [PubMed: 10342767]
47. Simmons AH, Michal CA, Jelinski LW. Science. 1996; 271:84–87. [PubMed: 8539605]
48. Blackledge TA, Hayashi CY. J Exp Biol. 2006; 209:2452–2461. [PubMed: 16788028]
49. Work RW. Text Res J. 1977; 47:650.
50. Work RW. J Exp Biol. 1985; 118:379.
51. Gosline JM, Denny MW, DeMont ME. Nature. 1984; 309:551.

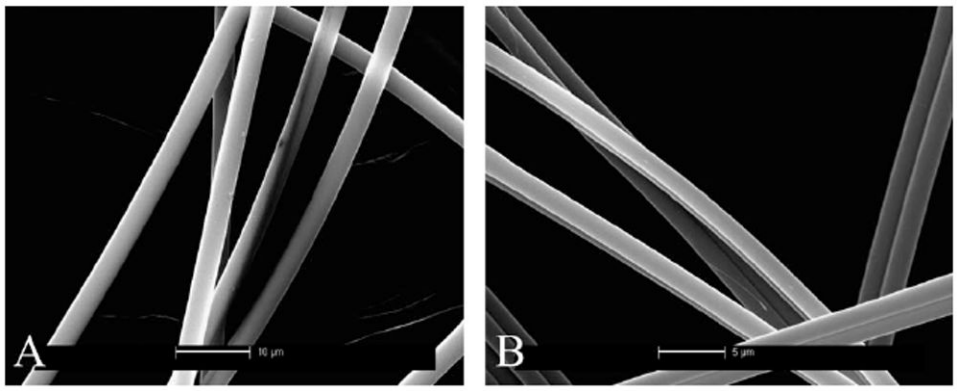

Fig. 1.
SEM images of MA and MiA fibers of *Nephila clavipes* (A and B respectively). Scales in the images are 10 μm for the MA and 5 μm MiA silks.

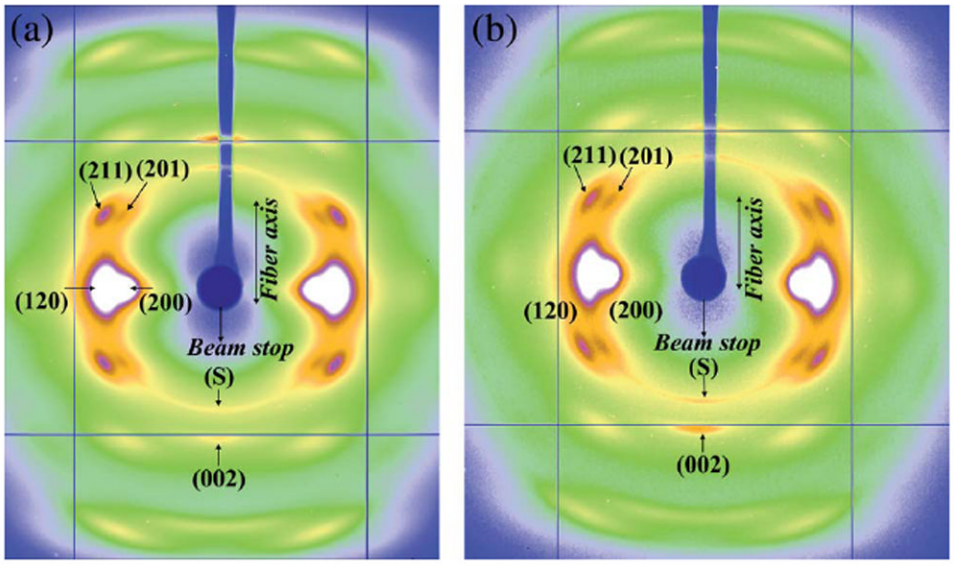

Fig. 2.

(a) WAXD pattern of *Nephila clavipes* major ampullate silk. (b) WAXD pattern of *Nephila clavipes* minor ampullate silk.

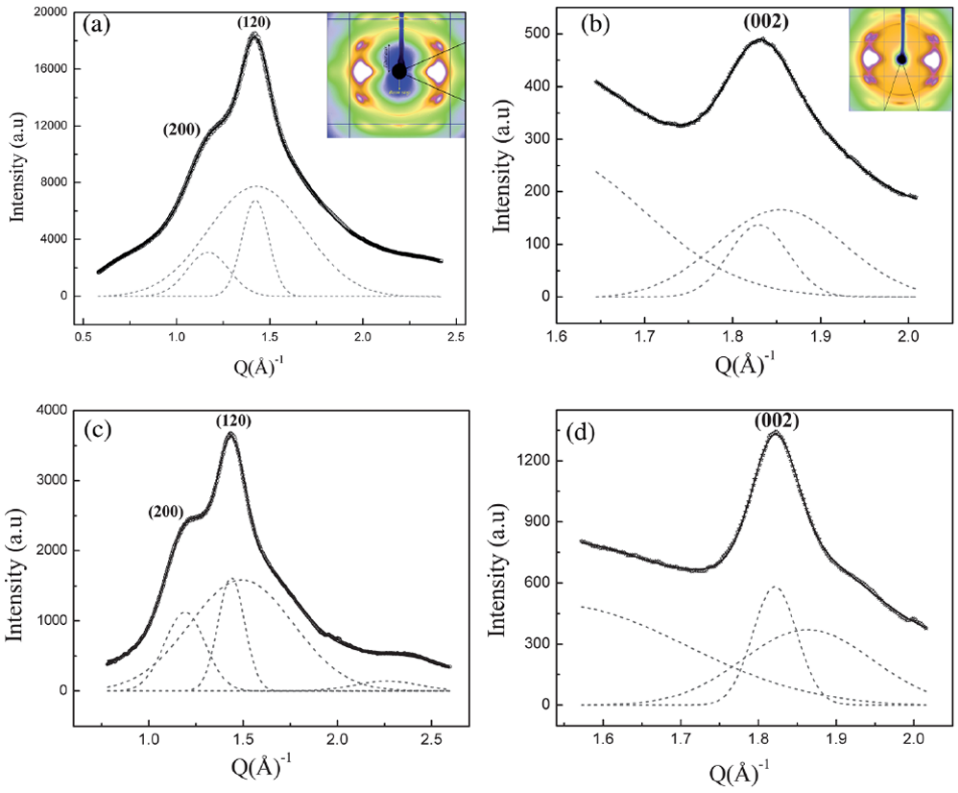

Fig. 3.

(a) 1D radial intensity profile of azimuthally integrated (120)/(200) equatorial peaks (○) data, Gaussian fits (---) for each peak and a broad Gaussian for the amorphous component for *Nephila clavipes* MA silk, (—) total fit. Inset shows the area selected for integration. (b) 1D radial intensity profile of azimuthally integrated (002) meridian peak (☆) data, Gaussian fits (---) for *Nephila clavipes* MA silk, (—) total fit. (c) 1D radial intensity profile of azimuthally integrated (120)/(200) equatorial peaks (○) data, Gaussian fits (---) for each peak and a broad Gaussian for the amorphous component for *Nephila clavipes* MiA silk, (—) total fit. (d) 1D radial intensity profile of azimuthally integrated (002) meridian peak (☆) data, Gaussian fits (---) for *Nephila clavipes* MiA silk, (—) total fit.

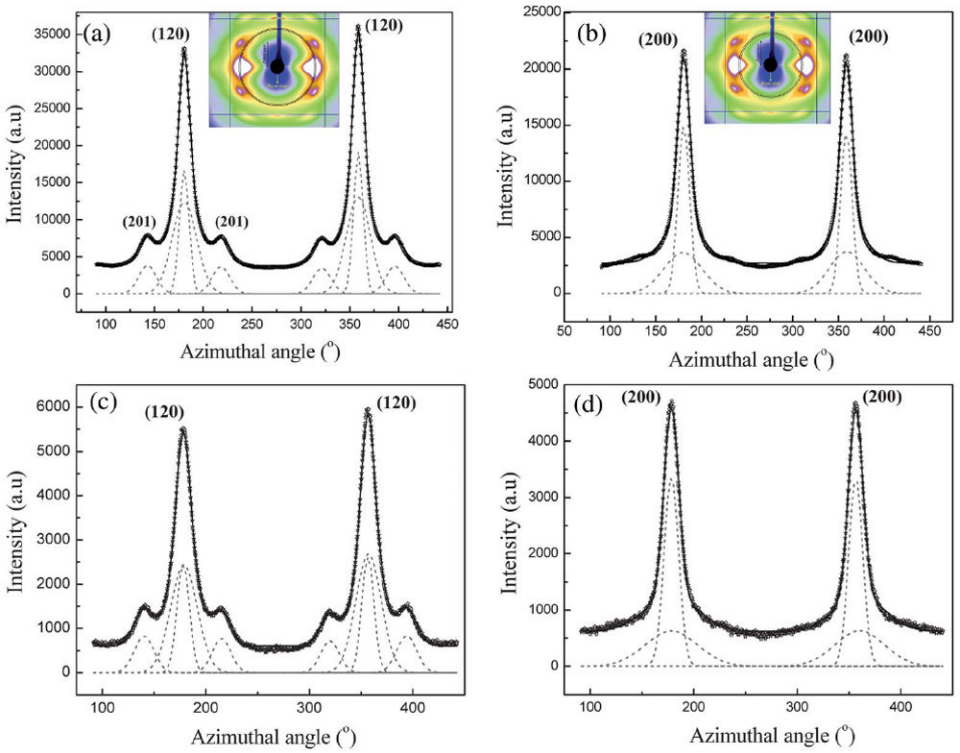

Fig. 4.

(a) 1D azimuthal intensity profile of the radially integrated (120) peak with Gaussian fits for *Nephila clavipes* MA silk. Inset shows the annular section chosen for the integration. (b) 1D azimuthal intensity profile of the radially integrated (200) peak with Gaussian fits for *Nephila clavipes* MA silk. (c) 1D azimuthal intensity profile of the radially integrated (120) peak with Gaussian fits for *Nephila clavipes* MiA silk. (d) 1D azimuthal intensity profile of the radially integrated (200) peak with Gaussian fits for *Nephila clavipes* MiA silk.

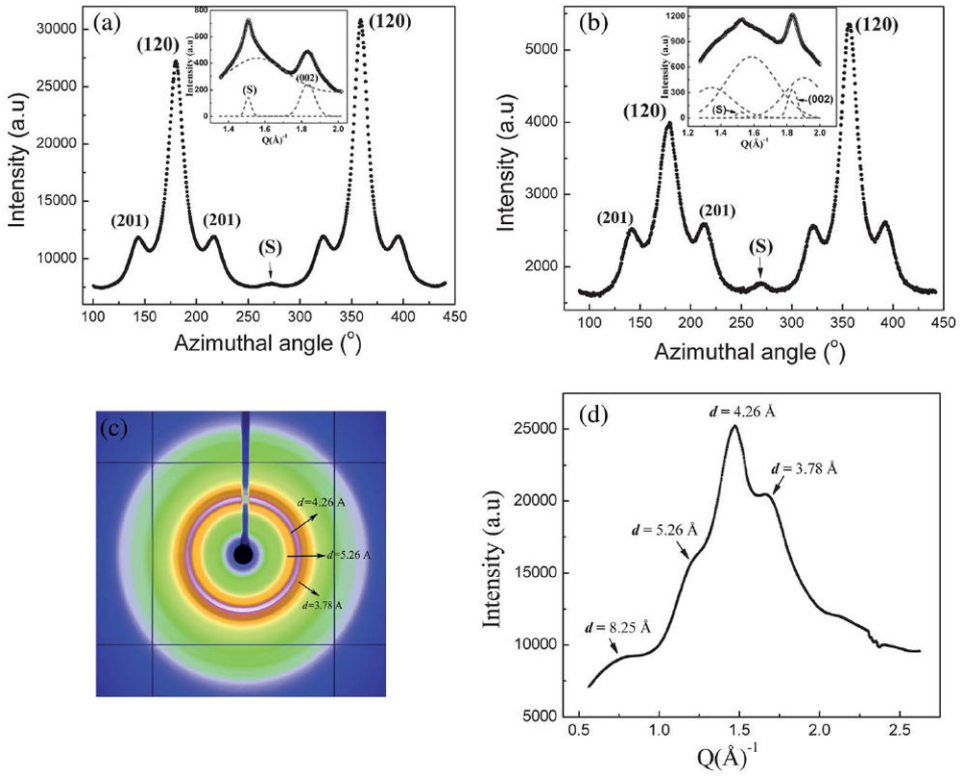

Fig. 5.

(a) 1D azimuthal intensity profile at the radial position of the superlattice peak (S) for *Nephila clavipes* MA silk. Inset shows the 1D radial intensity profile of the S peak along with the (002) peak. (b) 1D azimuthal intensity profile at the radial position of the superlattice peak (S) for *Nephila clavipes* MiA silk. Inset shows the 1D radial intensity profile of the S peak along with the (002) peak. (c) WAXD pattern of the dehydrated gland material of *Nephila clavipes* major ampullate gland. (d) 1D radial integration profile of the whole 2D pattern of the dehydrated gland material of *Nephila clavipes* major gland.

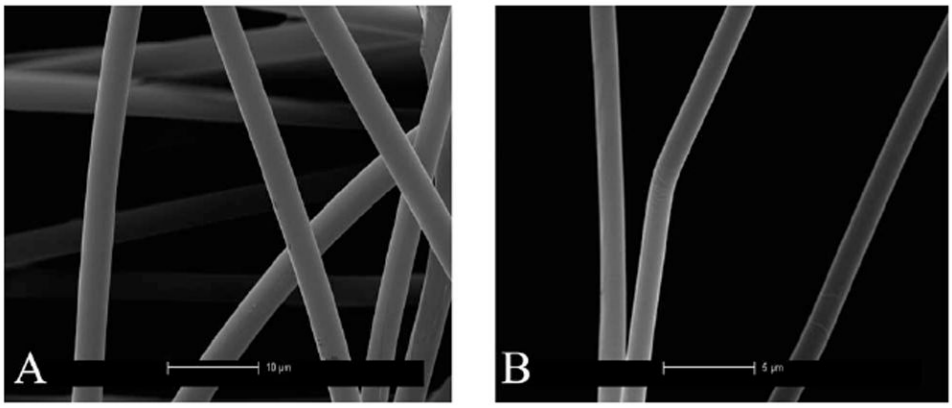

Fig. 6.
SEM images of MA and MiA fibers of fibers of *Argiope aurantia* (A and B respectively) Scales in the images are 10 μm for the MA and 5 μm MiA silks.

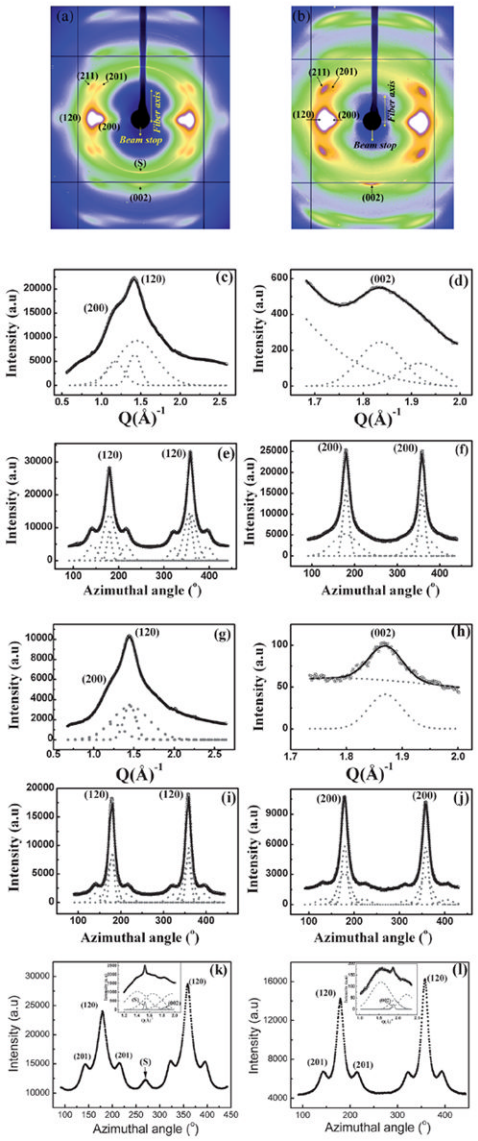

Fig. 7.

(a) WAXD pattern of *Argiope aurantia* major ampullate silk. (b) WAXD pattern of *Argiope aurantia* minor ampullate silk. (c) 1D radial intensity profile of azimuthally integrated (120)/(200) equatorial peaks (○) data, Gaussian fits (---) for each peak and a broad Gaussian for the amorphous component for *Argiope aurantia* MA silk, (—) total fit. (d) 1D radial intensity profile of azimuthally integrated (002) meridian peak (☆) data, Gaussian fits (---), (—) total fit. (e and f) 1D azimuthal intensity profile of the radially integrated (120) and (200) peaks respectively, with Gaussian fits. (g) 1D radial intensity profile of azimuthally integrated (120)/(200) equatorial peaks (○) data, Gaussian fits (---) for each peak and a broad Gaussian for the amorphous component for *Argiope aurantia* MiA silk, (—) total fit. (h) 1D radial intensity profile of azimuthally integrated (002) meridian peak (☆) data, Gaussian fits (---), (—) total fit. (i and j) 1D azimuthal intensity profile of the radially integrated (120) and (200) peaks respectively, with Gaussian fits. (k) 1D azimuthal intensity profile at the radial position of the superlattice peak (S) for *Argiope aurantia* MA silk. Inset shows the 1D radial intensity profile of the S peak along with the (002) peak. The S peak is stronger than the (002) peak. (l) 1D azimuthal intensity profile at the radial position of the

superlattice peak (S) for AA MiA silk. Inset shows the 1D radial intensity profile, the S peak is absent in *Argiope aurantia* MiA silk.

Table 1

d-spacings of the principal reflections for NC and AA, MA and MiA silks

***d*-spacing (Å)**	**(hkl)**	**I_{scaled} = $I/I_{max\ (120)}$ NC-MA**	***d*-spacing (Å)**	**I_{scaled} = $I/I_{max\ (120)}$ NC-MiA**	***d*-spacing (Å)**	**I_{scaled} = $I/I_{max\ (120)}$ AA-MA**	***d*-spacing (Å)**	**I_{scaled} = $I/I_{max\ (120)}$ AA-MiA**
2.084	(203/(213)/(123)	0.377	2.087	0.373	2.088	0.465	2.077	0.499
2.237	(103)/(013)/(113)	0.392	2.239	0.387	2.232	0.477	2.234	0.507
3.49	(002)	0.625	3.41	0.624	2.961	0.565	3.477	0.709
3.732	(211)	0.789	3.728	0.803	3.337	0.638	3.742	0.841
					3.726	0.832		
4.384	(120)	1	4.336	1	4.396	1	4.392	1
5.421	(200)	0.659	5.391	0.681	5.438	0.701	9.365	0.347
9.4		0.294	9.294	0.332	9.499	0.307		

Soft Matter. Author manuscript; available in PMC 2013 July 07.

Table 2

Herman's orientation function for NC & AA, MA and MiA silks

	f_{cryst}	$f_{oriented\text{-}amorphous}$	% Crystallinity	Crystallite size (nm)	$I_{(002)}/I_{(S\ pk\ @meridian)}$	Proline content (%)
NC-MA	0.980	0.808	28	*a*= 2.65 *b* = 3.97 *c* = 7.05	4.07	3.5
NC-MiA	0.975	0.758	44	*a* = 2.62 *b* = 4.02 *c* = 10.1	5.73	0.62
AA-MA	0.979	0.715	31	*a* = 2.45 *b* = 3.61 *c* = 6.76	0.79	9.92
AA-MiA	0.976	0.918	38	*a* = 2.14 *b* = 3.99 *c* = 9.24	S peak not present	0